

Long-term evolution of ocean eddy activity in a warming world

Received: 30 November 2021

Accepted: 18 August 2022

Published online: 29 September 2022

 Check for updates

Nathan Beech¹✉, Thomas Rackow², Tido Semmler¹, Sergey Danilov^{1,3}, Qiang Wang¹ and Thomas Jung^{1,4}

Mesoscale ocean eddies, an important element of the climate system, impact ocean circulation, heat uptake, gas exchange, carbon sequestration and nutrient transport. Much of what is known about ongoing changes in ocean eddy activity is based on satellite altimetry; however, the length of the altimetry record is limited, making it difficult to distinguish anthropogenic change from natural variability. Using a climate model that exploits a variable-resolution unstructured mesh in the ocean component to enhance grid resolution in eddy-rich regions, we investigate the long-term response of ocean eddy activity to anthropogenic climate change. Eddy kinetic energy is projected to shift poleward in most eddy-rich regions, to intensify in the Kuroshio Current, Brazil and Malvinas currents and Antarctic Circumpolar Current and to decrease in the Gulf Stream. Modelled changes are linked to elements of the broader climate including Atlantic meridional overturning circulation decline, intensifying Agulhas leakage and shifting Southern Hemisphere westerlies.

Since the advent of satellite altimetry, researchers have exploited the concept of geostrophy to characterize the movement of the near-surface ocean^{1–3}. By balancing the Coriolis force with the pressure gradient, geostrophic currents can be calculated until the Coriolis parameter becomes negligible near the equator⁴. These currents are accurate enough to identify both consistent, large-scale circulation features such as gyres and boundary currents and smaller short-lived phenomena such as eddies⁵. The major drivers of ocean eddies are barotropic and baroclinic instability that convert mean kinetic energy and available potential energy from the mean flow of ocean currents into eddy kinetic energy (EKE)^{6–8}. These mechanisms connect eddy-rich regions to the paths of major ocean surface flows including gyres and boundary currents, although other factors, such as bathymetry^{3,9} and wind stress¹⁰, also influence eddy activity. Eddies subsequently impact physical and biological ocean systems through ventilation^{11,12}, volume transport¹³, carbon sequestration¹⁴ and heat and nutrient transport^{15–17}, fuelling the interest in ocean eddy research.

Early altimetry studies were able to identify western boundary currents as eddy-rich regions and estimate their energy content,

spatial scale and movement during the first brief periods for which data were available^{1,2}. More recent altimetry studies have taken advantage of growing datasets to evaluate variability and change in ocean surface velocities and eddy fields and generally detect modest linear changes^{10,18–20}, although some caution that much longer datasets will be necessary for robust results²¹. Just as satellite altimetry overcame the spatial and temporal limitations of in situ velocity observations, modern numerical climate models can overcome the temporal limitations of the observational record by simulating datasets longer than the altimetry record will grow for generations to come. However, the length, resolution and ensemble size of model simulations are constrained by computational efficiency and resources.

In the sixth phase of the Coupled Model Intercomparison Project²² (CMIP6), the average ocean resolution is approximately 60 km (ref. ²³), which is insufficient to resolve eddies in most of the global ocean. At low latitudes, eddy-present simulations require resolutions of approximately 25 km or finer, and eddy-rich simulations require resolutions of approximately 10 km or finer. At higher latitudes,

¹Alfred Wegener Institute Helmholtz Center for Polar and Marine Research, Bremerhaven, Germany. ²European Centre for Medium-Range Weather Forecasts, Bonn, Germany. ³Mathematics and Logistics, Jacobs University, Bremen, Germany. ⁴Department of Physics and Electrical Engineering, University of Bremen, Bremen, Germany. ✉e-mail: nathan.beech@awi.de

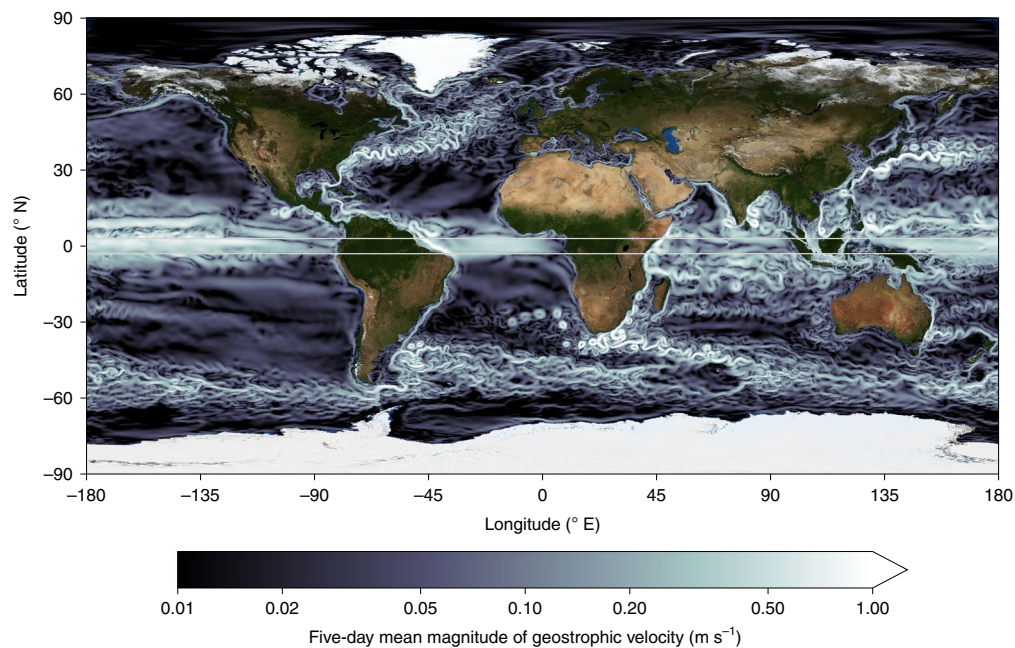


Fig. 1 | Magnitudes of simulated geostrophic ocean surface velocities. A snapshot of geostrophic velocities calculated from sea surface heights simulated by AWI-CM-1-1-MR for CMIP6 historical simulations. The equatorial region

highlighted by grey lines (3° S to 3° N) is replaced with monthly mean velocity after linear interpolation to five-day mean time steps. Background image: NASA Earth Observatory.

where the local Rossby radius decreases and the size of ocean eddies shrinks accordingly, resolution demands become greater and even at eddy-rich and eddy-present resolutions, certain characteristics of eddies, including size and frequency, may still not be entirely captured by models²⁴.

In the face of limited computing resources and a demand for finer resolutions in ocean modelling, it is advantageous to reduce net computational effort relative to grid resolution. Existing modelling studies of ocean eddies tend to rely on idealized simulations¹⁰, ocean-only models^{25,26} or simulations limited in spatial coverage, ensemble size or length^{15,27–29}. In contrast, the Finite Element Sea-ice Ocean Model^{30,31} (FESOM) enables the concentration of computational resources via an unstructured mesh with which the spatial resolution of regions can be adjusted based on relevance to the global climate system and the needs of the user^{31–33}. This variable-resolution capability, along with excellent scalability³⁴, allows FESOM to regionally resolve small-scale ocean processes before similar simulations using regular grids can feasibly achieve the necessary resolution throughout the global ocean. FESOM participated in CMIP6 and contributed to the Intergovernmental Panel on Climate Change's Sixth Assessment Report as the ocean component of the coupled model AWI-CM-1-1-MR (refs. ^{35,36}), uniquely facilitating eddy-rich and eddy-present ocean resolutions in selected regions (Extended Data Figs. 1 and 2) within the already computationally demanding CMIP framework.

In this study, the CMIP6 simulations from AWI-CM-1-1-MR (refs. ^{35,36}), in which fundamental aspects of mesoscale eddy activity are remarkably well reproduced (Fig. 1), are used to assess historical and future changes in EKE given ongoing anthropogenic climate change. Methodology is tailored to the dataset to address challenges in analysing EKE within a changing climate. Consistency with the CMIP framework will allow results to be interpreted in the context of more comprehensive climate change research, such as the Intergovernmental Panel on Climate Change assessment reports, and a wealth of other climate change projections. The satellite altimetry record is put into the perspective of prolonged warming under historical emissions, and a projected emissions scenario and potential physical mechanisms behind simulated EKE changes are investigated.

Model performance and contextualization of observations

AWI-CM-1-1-MR reproduces observed EKE with remarkable accuracy for a CMIP6 model (Fig. 2a,b), most of which are eddy parameterizing²³. The spatial distribution is particularly well represented compared with observed EKE from a gridded satellite altimetry product (Fig. 2b), with regions of high-eddy activity concentrated along well-known ocean surface currents, including western boundary currents and ocean gyres, and a band of high-eddy activity represented in the tropics. Nonetheless, there are some regions in which EKE representation is noticeably different, such as the lower-than-observed simulated EKE corresponding to preconditioned regions of insufficient grid resolution around the East Australian Current and the Mozambique Channel. EKE distribution in the North Atlantic follows a path more zonal than is observed, which reflects the common challenges of Gulf Stream separation bias and North Atlantic current representation in climate models often attributed to grid resolution^{37,38}. In FESOM, the path can be improved with higher model resolution, although this is not the only factor³³. Because the ocean grid of AWI-CM-1-1-MR can only be considered eddy-present in large parts of major ocean currents (Extended Data Figs. 1 and 2), it can be expected that modelled EKE is lower than is observed by satellites, ranging from about 51% of observed EKE in the Antarctic Circumpolar Current (ACC) to about 82% in the Kuroshio Current (Supplementary Table 1). The magnitude of EKE variability is more accurately resolved (Supplementary Table 2) but again underrepresents observations. This underrepresentation must be acknowledged as a limitation when interpreting EKE change within these simulations.

The internal variability of the modelled EKE ensemble over the 28-year observational period suggests that the signal-to-noise ratio of anthropogenic changes to natural variability is still quite low (Fig. 3). Despite this, previous analysis of the altimetry record has identified statistically significant positive linear trends in the Agulhas, ACC and Brazil and Malvinas currents (BMC), and non-significant increases have been identified in the Gulf Stream and Kuroshio²⁰. To contextualize these observations, simulated Gulf Stream EKE during the observational period (1993–2020) changes very little, and the ensemble spread includes both positive and negative trends (Extended Data Fig. 3),

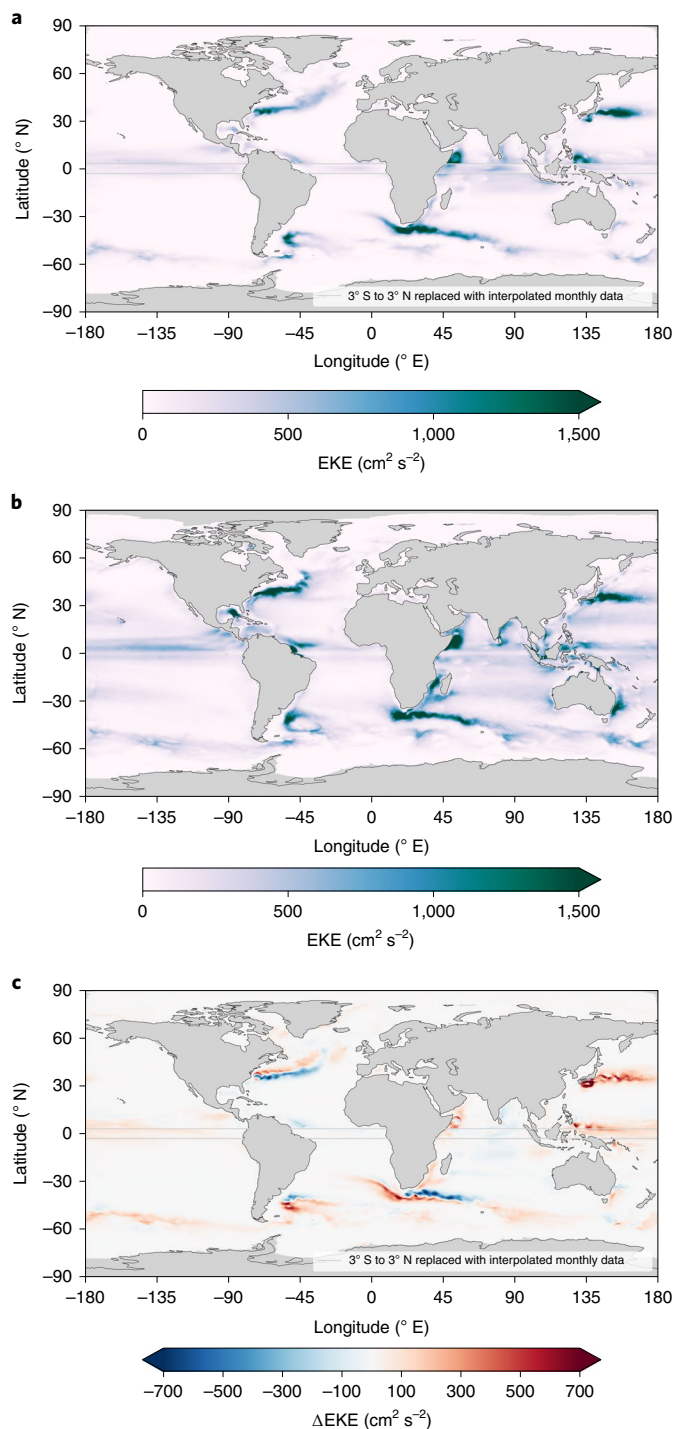


Fig. 2 | Simulated and observed eddy kinetic energy patterns in the global ocean. a, Ensemble mean of simulated eddy kinetic energy during the observational period (1993–2020). **b**, Observed mean eddy kinetic energy (1993–2020). **c**, Change in ensemble mean of eddy kinetic energy between historical (1860–1949) and projected (2061–2090) periods with GHG forcing, according to SSP3–7.0.

reinforcing the insignificance of observed trends. The simulated EKE rise in the Kuroshio Current and BMC accelerates between the observational period and the subsequent projections (Extended Data Fig. 3), suggesting that observed EKE rise, whether significant or not, is not yet fully representative of long-term change. In the Agulhas region, EKE rise during the observed period decreases drastically in the following projected period, and only in the ACC is EKE change consistent throughout

the observed period and the long-term projections (Extended Data Fig. 3). Thus, in most regions, the modelled results indicate that the length of the observational record is still insufficient to capture long-term EKE changes either in character or magnitude and that care must be taken when distinguishing anthropogenic change from natural variability. Differences in the magnitude of linear change over the observed and projected periods could be indicative of a nonlinear EKE response to anthropogenic forcing, nonlinear GHG emissions, high natural variability or a time of emergence of change occurring at some point during the observational period.

Eddy kinetic energy change

Unlike model performance and the coherence of simulated EKE change during the altimetry era, the long-term modelled projections of EKE cannot be validated using observations. Instead, they must be interpreted with respect to current knowledge of ocean circulation and climate dynamics, applicable historical analogues and the published literature. The following paragraphs will link the long-term projections of EKE to the potential physical mechanisms responsible for them, and by doing so, solidify the reliability of the modelled results.

The Gulf Stream

In addition to the widely anticipated poleward shift of the Gulf Stream^{39–41}, the North Atlantic is projected to experience a major decrease in eddy activity over the twenty-first century (Fig. 3c). After a slight increase between the mid-twentieth century and the present, the ensemble mean of simulated EKE falls by approximately 2.5 standard deviations (σ) by 2090 at a rate of $-0.84 \sigma \text{ } ^\circ\text{K}^{-1}$ after mean global surface temperature (MGST) surpasses a $1 \text{ } ^\circ\text{K}$ anomaly threshold (Figs. 3a and 4a). One explanation for this decrease could be simulated Atlantic Meridional Overturning Circulation (AMOC) weakening⁴², which is present in much of the CMIP6 ensemble⁴³, including AWI-CM-1-I-MR (ref. 36) (Extended Data Figs. 4 and 5) and would reduce volume transport through the upper Gulf Stream where eddy activity occurs. The modelled dataset reveals a relationship between unfiltered AMOC and Gulf Stream EKE of $0.23 \sigma \text{ Sv}^{-1}$ (Extended Data Fig. 6), which, while significant, explains relatively little of the simulated interannual EKE variability in the Gulf Stream ($R^2 = 0.10$; Extended Data Fig. 6). Isolating low-frequency variability reveals a much stronger relationship of $0.36 \sigma \text{ Sv}^{-1}$ ($R^2 = 0.24$; Extended Data Fig. 6), which suggests that EKE measured from satellite altimetry could be a fingerprint of long-term changes in AMOC strength.

The Kuroshio Current

Interestingly, the Kuroshio is the only western boundary current for which the eddy field is not projected to shift poleward (Fig. 2c). This has some precedence in the existing literature, as there is contradictory evidence regarding overall spatial change in the Kuroshio^{39,44}, and it exhibits a weaker poleward shift relative to natural variability compared with other western boundary currents⁴⁰. This exception may also be due to a disconnection between surface and subsurface flow in the region, which diverged in 2002, after which only the subsurface continued to shift poleward⁴⁵. Change in the magnitude of Kuroshio EKE is clearer; the ensemble mean increases by approximately 4σ by 2090 and rises at a rate of $1.56 \sigma \text{ } ^\circ\text{K}^{-1}$ after MGST surpasses a $1 \text{ } ^\circ\text{K}$ anomaly threshold (Figs. 3b and 4b).

Notably, individual ensemble members exhibit periods of EKE in the Kuroshio substantially higher than the mean (for example, 2040–2050; Fig. 3b). Closer inspection of these periods reveals that changes between the Large Meander (LM) and Non-Large Meander (NLM) states of the Kuroshio^{39,46}, result in large velocity anomalies along both paths. These anomalies are the result of a spatial oscillation in mean flow but can be misinterpreted as time-varying flow due to the bimodal nature of the path of the Kuroshio (Supplementary Video 1). It should, therefore, be concluded that the intermittent periods of particularly intense EKE

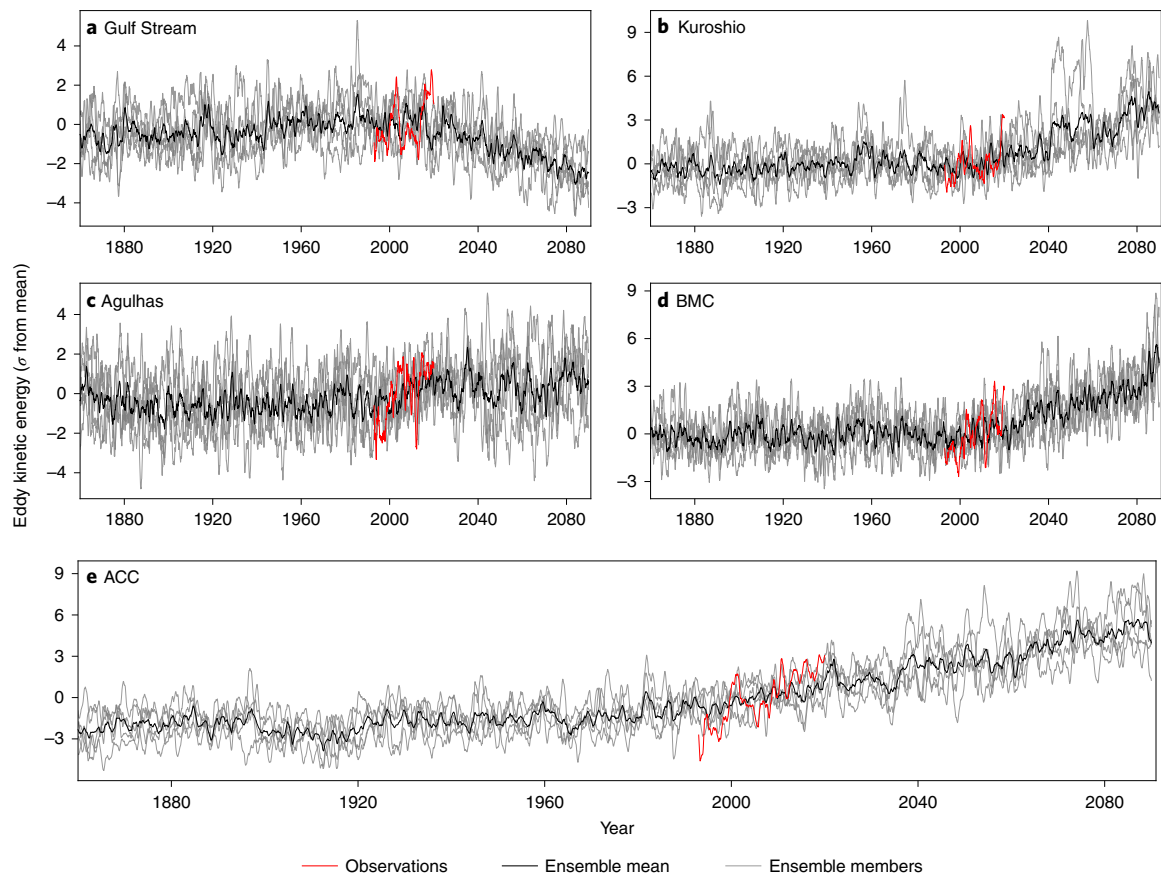


Fig. 3 | Regional eddy kinetic energy change. Observed and simulated area-integrated regional eddy kinetic energy anomalies normalized relative to conditions during the observational period (1993–2020). Sigma (σ) represents

the standard deviation of conditions during the observational period (1993–2020) in each basin, respectively. **a**, The Gulf Stream. **b**, The Kuroshio Current. **c**, The Agulhas Current. **d**, BMC. **e**, ACC.

in the Kuroshio (Fig. 3a) are not entirely representative of eddy activity, nor is the region of high EKE along the paths of the LM and NLM realistic (Fig. 2c). The same analysis of the observational dataset, which defines anomalies with respect to a reference period, reveals a similar pattern of intermittent eddy activity along the paths of the LM and NLM (Fig. 3a and Supplementary Video 2). This suggests that seemingly unrealistic high EKE in regions with spatially oscillating mean flow is an issue affecting methodology rather than the dataset. While distinguishing these periods of apparently high EKE from the overall eddy activity in the Kuroshio, there still appears to be an increase in the magnitude of EKE (Figs. 3b and 4b). Such an increase can be attributed to greater volume transport through the upper-layer Kuroshio, which increased by approximately 1 Sv, or 8% of the historical mean over the course of the simulations (Extended Data Figs. 4 and 5 and Supplementary Table 4). This response has been predicted in the context of climate change using both numerical models and observations as a result of intensified local wind stress⁴⁷, ocean stratification⁴⁸ and tropical cyclones⁴⁹. Further analysis of the relationship between Kuroshio volume transport and EKE is confounded by the correlation between high (low) volume transport and the LM (NLM) path⁵⁰, and by extension, the aforementioned unrepresentatively high EKE values. For this reason, correlation between EKE and volume transport in the Kuroshio is not investigated.

The Agulhas Current

Modelled results show the eddy-rich region corresponding to the Agulhas Current shifting westward and poleward as warming continues (Fig. 2c). A positive trend of $0.29 \sigma \text{ } ^\circ\text{K}^{-1}$ is identified in the Agulhas (Fig. 4c), and while statistically significant, temperature rise is a poor predictor of local EKE ($R^2 = 0.03$). Despite relatively little change in magnitude

(Fig. 3c), EKE change in the Agulhas region can provide insight into local ocean circulation. The substantial projected intensification of eddy activity from the southern coast of Africa into the South Atlantic appears to be indicative of Agulhas leakage: the transport of warm, salty Indian Ocean water into the South Atlantic. Agulhas leakage tends to take the form of mesoscale activity^{51,52}, and simulated leakage approximated by volume transport (Supplementary Table 4) increases by approximately 6 Sv, or 28% of the historical mean, over the course of the simulations (Extended Data Figs. 4 and 5).

Increased Agulhas leakage has been identified as a result of historical climate change using both hindcast modelling simulations⁵³ and observations^{54,55}, and prior modelling studies have projected further increases as climate change continues⁵⁶. Proxy records have also linked increased inter-ocean exchange through the Agulhas to periods of rapid warming during transitions from glacial to interglacial conditions⁵⁷, which could be analogous to anthropogenic climate change. Heat and salinity transported from the Indian Ocean to the South Atlantic by Agulhas leakage contribute to AMOC strength^{58–61}, but the decline of AMOC in our simulations (Extended Data Figs. 4 and 5 and Supplementary Table 4) indicates that the overall effect of anthropogenic climate change on AMOC will be negative. High Agulhas leakage and a southwestward shift of the Agulhas retroflection have been associated with lower overall Agulhas transport⁶². Our simulations reinforce this association, as Agulhas volume transport is projected to decrease by 10 Sv or 15% of mean historical transport. EKE change in the Agulhas can be attributed to the poleward shift and intensification of Southern Hemisphere westerly winds^{53,55,63,64}, and this, too, is consistent with the modelled dataset in which mean zonal surface wind decreases between approximately 25–45° S and increases south of approximately 45° S (Extended Data Fig. 7).

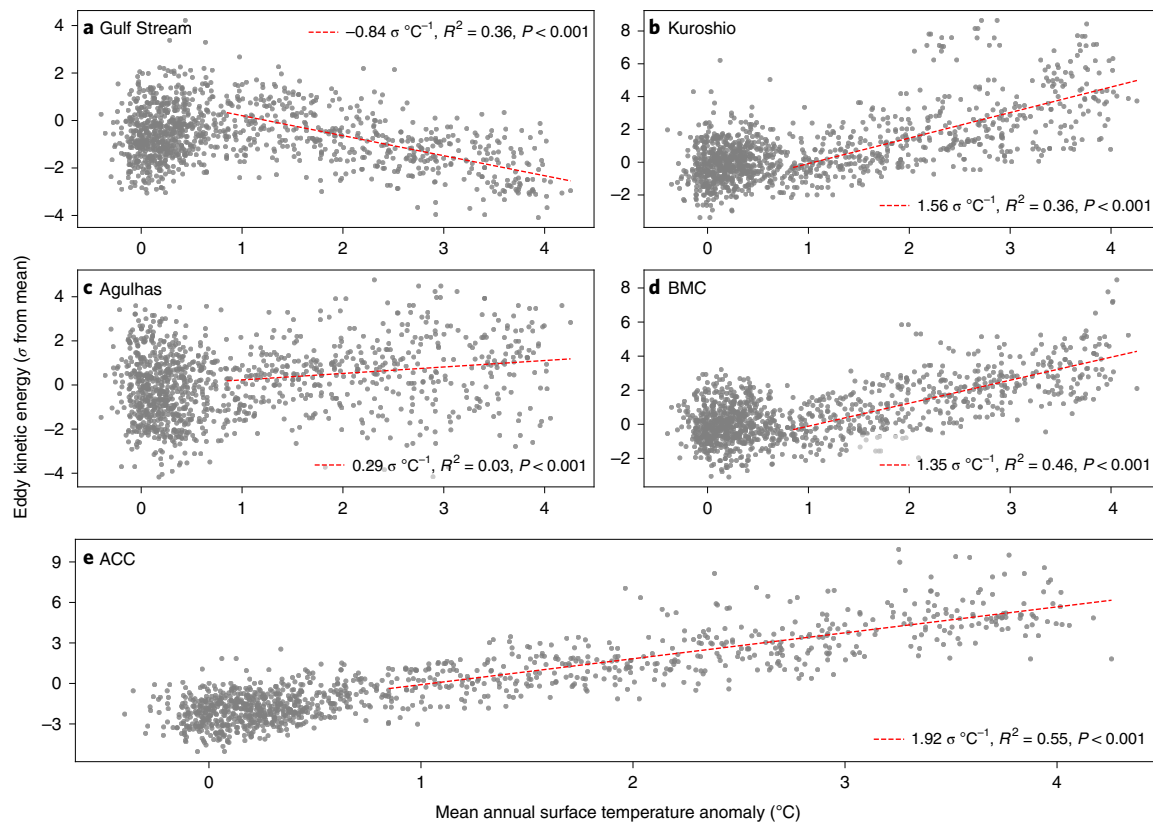


Fig. 4 | Regional eddy kinetic energy change relative to temperature rise.

Simulated area-integrated regional eddy kinetic energy anomalies normalized relative to conditions during the observational period (1993–2020) and plotted relative to simulated mean annual surface temperature anomalies from mean

conditions between 1850 and 1899. Linear trends are fit to EKE anomalies after an 11-year running mean of mean annual surface temperature anomalies surpasses 1 °K. **a**, The Gulf Stream. **b**, The Kuroshio Current. **c**, The Agulhas Current. **d**, BMC. **e**, ACC.

The BMC

EKE in the BMC basin is projected to shift southward (Fig. 2c) and increase in magnitude by approximately 5 σ by 2090 (Fig. 3d) at a rate of approximately 1.35 σ °K⁻¹ (Fig. 4d). The spatial EKE shift is corroborated by analysis of the relatively short observational record, which has already detected a modest southward shift of the currents in this region^{65–67}. Independent numerical experiments have further corroborated this result^{68,69} and attribute the spatial shift of the BMC to a weakening of the Malvinas Current as Southern Hemisphere westerlies shift south. The simulations considered here produce similar conditions; westerlies shift south over the Southern Ocean (Extended Data Fig. 7), and volume transport through the Malvinas Current decreases by approximately 11 Sv, or 15% of the historical mean (Extended Data Figs. 4 and 5 and Supplementary Table 4). Observational studies of the intensity of transport through the BMC have generally found insignificant or no trends^{65,66}, but palaeoclimatic evidence of ocean transport in the region may set a precedent for rising EKE. Sediment core proxy records have linked periods of high volume transport in the Brazil Current to weak AMOC^{70,71}, which is consistent with the approximately 3 Sv, or 17% decline of simulated AMOC in these simulations (Extended Data Figs. 4 and 5 and Supplementary Table 4). AMOC is a relatively strong indicator of BMC EKE, particularly considering low-frequency variability ($R^2 = 0.53$ and Extended Data Fig. 6). The mechanism for this change theorized from proxy evidence is that as the northward removal of warm, salty water from the southern and tropical Atlantic lessens, transport shifts towards a southward route in response to a build-up of heat and salinity^{70–73}. Once again, the modelled dataset supports this hypothesis; volume transport through the North Brazil Current decreases by approximately 2 Sv, or 6% of the historical mean, and increases through the Brazil Current by approximately 2 Sv, or 4% of the historical mean, over the course of the

simulations (Extended Data Figs. 4 and 5 and Supplementary Table 4). Linear regression reveals significant relationships between BMC EKE and Brazil and North Brazil Current volume transport, particularly after isolating low-frequency variability (Extended Data Fig. 6).

The ACC

In the ACC, intensification of strong atmospheric westerly winds⁷⁴ has already imparted more energy to the surface ocean via wind stress⁷⁵. This has increased Southern Ocean eddy activity while transport has remained stable according to the theory of eddy saturation⁷⁶. Our projections suggest this will continue throughout the twenty-first century (Extended Data Fig. 7), resulting in ensemble mean EKE approximately 6 σ greater than the observational period mean by 2090 (Fig. 3e). EKE is projected to rise at a rate of 1.92 σ °K⁻¹ after the 1 °K MGST anomaly threshold (Fig. 4e). Meanwhile, transport through the Drake Passage decreased by approximately 2 Sv, or 1% of historical mean annual transport (Extended Data Figs. 4 and 5 and Supplementary Table 4). Although a statistically significant change, this is most likely physically inconsequential to the local conditions, suggesting that the ACC simulated by FESOM is at or near its eddy-saturated state, where stronger winds no longer increase mean transport but instead intensify eddy activity. Interestingly, the ACC is the only basin considered here where simulated EKE rise begins before the start of the observational period (Fig. 3e), suggesting that observed trends here should already reflect long-term change. Indeed, simulated ACC EKE rises at approximately the same rate both during and after the observational period (Extended Data Fig. 3). However, it has been shown that EKE rise in response to wind stress along the ACC is greater in higher-resolution models⁷⁶, meaning EKE rise could be even more intense than these projections if a higher-resolution mesh is used.

Conclusions

Analysis of EKE in the world's oceans has historically been limited by the length of the satellite altimetry record and the computational challenge of modelling long time series at eddy-present resolutions. AWI-CM-1-1-MR, and specifically the ocean component, FESOM, contends with these challenges using a highly scalable dynamical core, along with an unstructured mesh and variable-resolution ocean grid. As a result, AWI-CM-1-1-MR's CMIP6 contribution is able to reproduce key features of global eddy activity, creating a unique opportunity to investigate how eddy activity might change in a warming world. Although AWI-CM-1-1-MR's unique characteristics have made this study possible, it will be essential for future work to corroborate the results using a diverse model ensemble.

Our analyses of CMIP6 simulations from AWI-CM-1-1-MR reveal pronounced long-term changes in projected EKE on a global scale. Early indications of these changes may be present in the observational record²⁰, but EKE changes in most eddy-rich regions do not yet appear to be wholly representative of long-term change either in character or magnitude. Nonetheless, the observational record is generally not contradictory to our results because modelled EKE change during the observational period is also not yet reflective of long-term projections in most regions. Importantly, the onset of EKE changes relative to both time and MGST rise suggests that these changes should become increasingly clear relatively quickly as the observational record grows, making the altimetry dataset a crucial tool for evaluating these projections. Several of the long-term modelled projections reflect changes that have begun to appear in the observational record or other existing literature. A poleward shift of eddy activity follows the poleward shift of many major ocean currents expected in a warming climate^{39,40,44}. The ACC appears eddy-saturated as intensifying Southern Hemisphere westerlies increase eddy activity and ACC volume transport remains relatively stable⁷⁶. Lower transport through the Agulhas Current reflects a more southwestward retroflexion and more Agulhas leakage⁶². Eddy activity in the BMC shifts south while the strength of the Malvinas Current decreases and Southern Hemisphere westerlies shift south. Other results can generally be reinforced by anticipated anthropogenic impacts on ocean circulation. Decreasing EKE in the North Atlantic occurs concurrently with the widely anticipated decline of AMOC^{41–43}. Substantial growth of Kuroshio EKE occurs in conjunction with an anticipated strengthening of Kuroshio volume transport^{47–49}. Increased EKE in the southeastern Atlantic reflects greater Agulhas leakage, which is anticipated in a warming world based on palaeoclimatic and modelled evidence^{53–55,57}. Intensification of BMC EKE reflects a shift of thermohaline circulation in the Atlantic towards a southern route, consistent with model and palaeoclimatic evidence^{70–73}. The representation of various anticipated impacts of anthropogenic climate change by modelled EKE suggests that EKE discerned from satellite data could be a useful proxy for large-scale climatic changes that is more conveniently observed than in situ monitoring of ocean velocities or overturning circulation.

Online content

Any methods, additional references, Nature Research reporting summaries, source data, extended data, supplementary information, acknowledgements, peer review information; details of author contributions and competing interests; and statements of data and code availability are available at <https://doi.org/10.1038/s41558-022-01478-3>.

References

- Cheney, R. E., Marsh, J. G. & Beckley, B. D. Global mesoscale variability from collinear tracks of SEASAT altimeter data. *J. Geophys. Res.: Oceans* **88**, 4343–4354 (1983).
- Menard, Y. Observations of eddy fields in the northwest Atlantic and northwest Pacific by SEASAT altimeter data. *J. Geophys. Res.* **88**, 1853–1866 (1983).
- Heywood, K. J., McDonagh, E. L. & White, M. A. Eddy kinetic energy of the North Atlantic subpolar gyre from satellite altimetry. *J. Geophys. Res.: Oceans* **99**, 22525–22539 (1994).
- Lagerloef, G. S., Mitchum, G. T., Lukas, R. B. & Niiler, P. P. Tropical Pacific near-surface currents estimated from altimeter, wind, and drifter data. *J. Geophys. Res.: Oceans* **104**, 23313–23326 (1999).
- Chelton, D. B., Schlax, M. G. & Samelson, R. M. Global observations of nonlinear mesoscale eddies. *Prog. Oceanogr.* **91**, 167–216 (2011).
- Gill, A. E., Green, J. S. A. & Simmons, A. J. Energy partition in the large-scale ocean circulation and the production of mid-ocean eddies. *Deep Sea Res. Oceanogr. Abstr.* **21**, 499–528 (1974).
- Ogata, T. & Masumoto, Y. Interannual modulation and its dynamics of the mesoscale eddy variability in the southeastern tropical Indian Ocean. *J. Geophys. Res.: Oceans* <https://doi.org/10.1029/2010JC006490> (2011).
- Constantinou, N. C. & Hogg, A. M. Eddy saturation of the Southern Ocean: a baroclinic versus barotropic perspective. *Geophys. Res. Lett.* **46**, 12202–12212 (2019).
- Endoh, T. & Hibiya, T. Numerical simulation of the transient response of the Kuroshio leading to the large meander formation south of Japan. *J. Geophys. Res.: Oceans* **106**, 26833–26850 (2001).
- Hogg, A. M. et al. Recent trends in the Southern Ocean eddy field. *J. Geophys. Res.: Oceans* **120**, 257–267 (2015).
- Lachkar, Z., Orr, J. C., Dutay, J. & Delecluse, P. On the role of mesoscale eddies in the ventilation of Antarctic intermediate water. *Deep Sea Res. Part I* **56**, 909–925 (2009).
- MacGilchrist, G. A., Marshall, D. P., Johnson, H. L., Lique, C. & Thomas, M. Characterizing the chaotic nature of ocean ventilation. *J. Geophys. Res.: Oceans* **122**, 7577–7594 (2017).
- Wang, Y., Claus, M., Greatbatch, R. J. & Sheng, J. Decomposition of the mean barotropic transport in a high-resolution model of the North Atlantic Ocean. *Geophys. Res. Lett.* **44**, 537–546 (2017).
- Sallée, J.-B., Matear, R. J., Rintoul, S. R. & Lenton, A. Localized subduction of anthropogenic carbon dioxide in the Southern Hemisphere oceans. *Nat. Geosci.* **5**, 579–584 (2012).
- Crews, L., Sundfjord, A., Albreetsen, J. & Hattermann, T. Mesoscale eddy activity and transport in the Atlantic water inflow region north of Svalbard. *J. Geophys. Res.: Oceans* **123**, 201–215 (2018).
- Falkowski, P., Ziemann, D., Kolber, Z. & Bienfang, P. K. Role of eddy pumping in enhancing primary production in the ocean. *Nature* **352**, 55–58 (1991).
- Oschlies, A. & Garçon, V. Eddy-induced enhancement of primary production in a model of the North Atlantic Ocean. *Nature* **394**, 266–269 (1998).
- Ding, M., Lin, P., Liu, H., & Chai, F. Increased eddy activity in the northeastern Pacific during 1993–2011. *J. Climate* <https://doi.org/10.1175/JCLI-D-17-0309.1> (2017).
- Martinez-Moreno, J., Hogg, A. M., Kiss, A. E., Constantinou, N. C. & Morrison, A. K. Kinetic energy of eddy-like features from sea surface altimetry. *J. Adv. Modeling Earth Syst.* **11**, 3090–3105 (2019).
- Martinez-Moreno, J. et al. Global changes in oceanic mesoscale currents over the satellite altimetry record. *Nat. Clim. Change* **11**, 397–403 (2021).
- Chi, L., Wolfe, C. L. & Hameed, S. Has the Gulf Stream slowed or shifted in the altimetry era? *Geophys. Res. Lett.* **48**, e2021GL093113 (2021).
- Eyring, V. et al. Overview of the Coupled Model Intercomparison Project Phase 6 (CMIP6) experimental design and organization. *Geosci. Model Dev.* **9**, 1937–1958 (2016).
- Hewitt, H. T. et al. Resolving and parameterising the ocean mesoscale in Earth system models. *Curr. Clim. Change Rep.* **6**, 137–152 (2020).

24. Moreton, S. M., Ferreira, D., Roberts, M. J. & Hewitt, H. T. Evaluating surface eddy properties in coupled climate simulations with ‘eddy-present’ and ‘eddy-rich’ ocean resolution. *Ocean Modell.* **147**, 101567 (2020).
25. Penduff, T. et al. Sea level expression of intrinsic and forced ocean variabilities at interannual time scales. *J. Clim.* **24**, 5652–5670 (2011).
26. Patara, L., Böning, C. W. & Biastoch, A. Variability and trends in Southern Ocean eddy activity in 1/12° ocean model simulations. *Geophys. Res. Lett.* **43**, 4517–4523 (2016).
27. Regan, H., Lique, C., Talandier, C. & Meneghello, G. Response of total and eddy kinetic energy to the recent spinup of the Beaufort Gyre. *J. Phys. Oceanogr.* **50**, 575–594 (2020).
28. Wang, Q. et al. Eddy kinetic energy in the Arctic Ocean from a global simulation with a 1-km Arctic. *Geophys. Res. Lett.* <https://doi.org/10.1029/2020GL088550> (2020).
29. Grist, J. P. et al. Future evolution of an eddy rich ocean associated with enhanced East Atlantic storminess in a coupled model projection. *Geophys. Res. Lett.* **48**, e2021GL092719 (2021).
30. Danilov, S., Kivman, G. & Schröter, J. A finite-element ocean model: principles and evaluation. *Ocean Modell.* **6**, 125–150 (2004).
31. Wang, Q. et al. The Finite Element Sea ice–Ocean Model (FESOM) v1.4: formulation of an ocean general circulation model. *Geosci. Model Dev.* **7**, 663–693 (2014).
32. Sein, D. V. et al. Designing variable ocean model resolution based on the observed ocean variability. *J. Adv. Model. Earth Syst.* **8**, 904–916 (2016).
33. Sein, D. V. et al. Ocean modeling on a mesh with resolution following the local Rossby radius. *J. Adv. Model. Earth Syst.* **9**, 2601–2614 (2017).
34. Koldunov, N. V. et al. Scalability and some optimization of the Finite-volume Sea ice–Ocean Model, Version 2.0 (FESOM2). *Geosci. Model Dev.* **12**, 3991–4012 (2019).
35. Semmler, T. et al. AWI AWI-CM 1.1 MR model output prepared for CMIP6 CMIP, version 2019–1219. Earth System Grid Federation <https://doi.org/10.22033/ESGF/CMIP6.359> (2018).
36. Semmler, T. et al. Simulations for CMIP6 With the AWI Climate Model AWI-CM-1.1. *J. Adv. Model. Earth Syst.* **12**, e2019MS002009 (2020).
37. Wang, C., Zhang, L., Lee, S. K., Wu, L. & Mechoso, C. R. A global perspective on CMIP5 climate model biases. *Nat. Clim. Change* **4**, 201–205 (2014).
38. Drews, A., Greatbatch, R. J., Ding, H., Latif, M. & Park, F. The use of a flow field correction technique for alleviating the North Atlantic cold bias with application to the Kiel Climate Model. *Ocean Dyn.* **65**, 1079–1093 (2015).
39. Yang, H. et al. Intensification and poleward shift of subtropical western boundary currents in a warming climate. *J. Geophys. Res.: Oceans* **121**, 4928–4945 (2016).
40. Yang, H. et al. Poleward shift of the major ocean gyres detected in a warming climate. *Geophys. Res. Lett.* **47**, e2019GL085868 (2020).
41. Caesar, L., Rahmstorf, S., Robinson, A., Feulner, G. & Saba, V. Observed fingerprint of a weakening Atlantic Ocean overturning circulation. *Nature* **556**, 191–196 (2018).
42. Bakker, P. et al. Fate of the Atlantic Meridional Overturning Circulation: strong decline under continued warming and Greenland melting. *Geophys. Res. Lett.* <https://doi.org/10.1002/2016GL070457> (2016).
43. Weijer, W., Cheng, W., Garuba, O. A., Hu, A., & Nadiga, B. T. CMIP6 models predict significant 21st century decline of the Atlantic Meridional Overturning Circulation. *Geophys. Res. Lett.* <https://doi.org/10.1029/2019GL086075> (2020).
44. Wu, L. et al. Enhanced warming over the global subtropical western boundary currents. *Nat. Clim. Change* **2**, 161–166 (2012).
45. Wu, B., Lin, X. & Yu, L. Poleward shift of the Kuroshio Extension front and its impact on the North Pacific subtropical mode water in the recent decades. *J. Phys. Oceanogr.* **51**, 457–474 (2021).
46. White, W. & McCreary, J. On the formation of the Kuroshio meander and its relationship to the large-scale ocean circulation. *Deep Sea Res. Oceanogr. Abstr.* **23**, 33–47 (1976).
47. Zhang, X., Wang, Q. & Mu, M. The impact of global warming on Kuroshio Extension and its southern recirculation using CMIP5 experiments with a high-resolution climate model MIROC4h. *Theor. Appl. Climatol.* **127**, 815–827 (2015).
48. Chen, C., Wang, G., Xie, S. & Liu, W. Why does global warming weaken the Gulf Stream but intensify the Kuroshio? *J. Clim.* **32**, 7437–7451 (2019).
49. Zhang, Y., Zhang, Z., Chen, D., Qiu, B. & Wang, W. Strengthening of the Kuroshio Current by intensifying tropical cyclones. *Science* **368**, 988–993 (2020).
50. Kawabe, M. Variations of current path, velocity, and volume transport of the Kuroshio in relation with the large meander. *J. Phys. Oceanogr.* **25**, 3103–3117 (1995).
51. Olson, D. B. & Evans, R. H. Rings of the Agulhas Current. *Deep Sea Res. Part A*, **33**, 27–42 (1986).
52. Lutjeharms, J. R. E. & Van Ballegooyen, R. C. The retroflection of the Agulhas Current. *J. Phys. Oceanogr.* **18**, 1570–1583 (1988).
53. Biastoch, A., Böning, C., Schwarzkopf, F. & Lutjeharms, J. Increase in Agulhas leakage due to poleward shift of Southern Hemisphere westerlies. *Nature* **462**, 495–498 (2009).
54. Rouault, M., Penven, P. & Pohl, B. Warming in the Agulhas Current system since the 1980s. *Geophys. Res. Lett.* <https://doi.org/10.1029/2009GL037987> (2009).
55. Backeberg, B., Penven, P. & Rouault, M. Impact of intensified Indian Ocean winds on mesoscale variability in the Agulhas system. *Nat. Clim. Change* **2**, 608–612 (2012).
56. Biastoch, A. & Böning, C. W. Anthropogenic impact on Agulhas leakage. *Geophys. Res. Lett.* **40**, 1138–1143 (2013).
57. Peeters, F. et al. Vigorous exchange between the Indian and Atlantic oceans at the end of the past five glacial periods. *Nature* **430**, 661–665 (2004).
58. Gordon, A. L. Inter-ocean exchange of thermocline water. *J. Geophys. Res.* **91**, 5037 (1986).
59. Weijer, W., de Ruijter, W. P. M., Dijkstra, H. A. & van Leeuwen, P. J. Impact of interbasin exchange on the Atlantic overturning circulation. *J. Phys. Oceanogr.* **29**, 2266–2284 (1999).
60. Knorr, G. & Lohmann, G. Southern Ocean origin for the resumption of Atlantic thermohaline circulation during deglaciation. *Nature* **424**, 532–536 (2003).
61. Biastoch, A., Böning, C. & Lutjeharms, J. Agulhas leakage dynamics affects decadal variability in Atlantic overturning circulation. *Nature* **456**, 489–492 (2008).
62. Van Sebille, E. V., Biastoch, A., Leeuwen, P. J. & Ruijter, W. P. A weaker Agulhas Current leads to more Agulhas leakage. *Geophys. Res. Lett.* <https://doi.org/10.1029/2008GL036614> (2009).
63. Cai, W. Antarctic ozone depletion causes an intensification of the Southern Ocean super-gyre circulation. *Geophys. Res. Lett.* <https://doi.org/10.1029/2005GL024911> (2006).
64. Bard, E. & Rickaby, R. Migration of the subtropical front as a modulator of glacial climate. *Nature* **460**, 380–383 (2009).
65. Goni, G. J., Bringas, F. & DiNezio, P. N. Observed low frequency variability of the Brazil Current front. *J. Geophys. Res.* **116**, C10037 (2011).
66. Lumpkin, R. & Garzoli, S. Interannual to decadal changes in the western South Atlantic surface circulation. *J. Geophys. Res.* <https://doi.org/10.1029/2010JC006285> (2011).

67. Drouin, K. L., Lozier, M. S. & Johns, W. E. Variability and trends of the South Atlantic subtropical gyre. *J. Geophys. Res.: Oceans* <https://doi.org/10.1029/2020JC016405> (2020).
68. Combes, V. & Matano, R. P. Trends in the Brazil/Malvinas confluence region. *Geophys. Res. Lett.* **41**, 8971–8977 (2014).
69. de Souza, M. M., Mathis, M. & Pohlmann, T. Driving mechanisms of the variability and long-term trend of the Brazil–Malvinas confluence during the 21st century. *Clim. Dyn.* **53**, 6453–6468 (2019).
70. Chiessi, C. M. et al. Variability of the Brazil Current during the late Holocene. *Palaeogeogr. Palaeoclimatol. Palaeoecol.* **415**, 28–36 (2014).
71. Meier, K. J. et al. Role of the tropical Atlantic for the interhemispheric heat transport during the last deglaciation. *Paleoceanogr. Paleoclimatol.* <https://doi.org/10.1029/2020PA004107> (2021).
72. Arz, H. W., Pätzold, J. & Wefer, G. The deglacial history of the western tropical Atlantic as inferred from high resolution stable isotope records off northeastern Brazil. *Earth Planet. Sci. Lett.* **167**, 105–117 (1999).
73. Zhu, C. & Liu, Z. Weakening Atlantic overturning circulation causes South Atlantic salinity pile-up. *Nat. Clim. Change* **10**, 998–1003 (2020).
74. Marshall, G. J. Trends in the Southern annular mode from observations and reanalyses. *J. Clim.* **16**, 4134–4143 (2003).
75. Allison, L. C., Johnson, H. L., Marshall, D. P. & Munday, D. R. Where do winds drive the Antarctic Circumpolar Current? *Geophys. Res. Lett.* <https://doi.org/10.1029/2010GL043355> (2010).
76. Munday, D. R., Johnson, H. L. & Marshall, D. P. Eddy saturation of equilibrated circumpolar currents. *J. Phys. Oceanogr.* **43**, 507–532 (2013).

Publisher's note Springer Nature remains neutral with regard to jurisdictional claims in published maps and institutional affiliations.

Open Access This article is licensed under a Creative Commons Attribution 4.0 International License, which permits use, sharing, adaptation, distribution and reproduction in any medium or format, as long as you give appropriate credit to the original author(s) and the source, provide a link to the Creative Commons license, and indicate if changes were made. The images or other third party material in this article are included in the article's Creative Commons license, unless indicated otherwise in a credit line to the material. If material is not included in the article's Creative Commons license and your intended use is not permitted by statutory regulation or exceeds the permitted use, you will need to obtain permission directly from the copyright holder. To view a copy of this license, visit <http://creativecommons.org/licenses/by/4.0/>.

© The Author(s) 2022

Methods

Model configuration

In AWI-CM-1-1-MR, FESOM version 1.4 employs a finite-element numerical core with a 46-layer ocean mesh varying in horizontal resolution from approximately 8 km to 80 km (ref. ³⁶). FESOM's horizontal grid uses triangular cells of variable size rather than a traditional rectangular grid to vary grid resolution³¹. The mesh used in these simulations was designed with particular consideration of observed sea surface height (SSH) variability as an indicator of dynamically active regions, and these regions are refined to sufficient resolution to simulate eddies based on the local Rossby radius of deformation^{32,33}. Thus, computational resources are allocated according to the observed presence of high local mesoscale activity, and resolution requirements for the simulation of mesoscale activity. While the design of the mesh is an attempt to make the best use of considerable computational resources needed to carry out full CMIP6 experiments, the nominal ocean resolution of 25 km, or approximately 0.83 million ocean nodes, cannot produce eddy-rich conditions across the entire globe under any configuration. Rather, the mesh configuration (Extended Data Fig. 1) compromises on resolution in large areas of relatively low eddy activity, but by doing so, local grid refinements can exceed $\frac{1}{2}$ of the local Rossby radius (R) along the paths of major ocean currents where high-eddy activity is observed. Importantly, $\frac{1}{2}R$ is a crucial threshold below which eddy-resolving conditions can be reached⁷⁷, although the characteristics of the simulated eddies, such as size, speed or longevity, may still not reflect observations²⁴, which could be a potential weakness in these simulations. Regions of high grid refinement are broader than observed regions of high SSH variability, to the extent that resources allow and steep resolution gradients are avoided; however, the potential for mesoscale activity to shift spatially beyond the refined grid regions remains a limitation of variable-resolution modelling. Outside of regions with sufficient resolution to simulate eddies, Gent–McWilliams eddy parameterization⁷⁸ is gradually introduced³¹. Information regarding the configuration of the atmospheric component and coupling is in the Supplementary Notes.

Data

Model data from AWI-CM-1-1-MR. This analysis considers a five-member ensemble of historical simulations and climate change projections³⁵ under shared socio-economic pathway (SSP) 3–7.0 following the CMIP6 standards²². Spin-up information for the simulations is available in the Supplementary Notes. Emissions scenarios in CMIP6 are based on a matrix of SSPs⁷⁹ and representative concentration pathways⁸⁰. SSP3–7.0 describes a relatively high-emissions scenario in which CO₂ levels are roughly doubled by the end of the century^{22,79,81}. Other models from the CMIP6 ensemble were considered for inclusion in this analysis, as explained in the Supplementary Notes, but it was concluded that the variable-resolution capabilities of AWI-CM-1-1-MR make it uniquely suited to this study.

Geostrophic ocean surface velocities were calculated using daily SSH with equations (1) and (2).

$$u = -\frac{g}{f} \frac{\partial \text{SSH}}{\partial y} \quad (1)$$

$$v = \frac{g}{f} \frac{\partial \text{SSH}}{\partial x} \quad (2)$$

where u and v refer to zonal and meridional geostrophic velocities, respectively, where x and y are the longitudinal and latitudinal positions, respectively, where g is gravitational acceleration and f is the Coriolis parameter.

The use of daily SSH enables EKE to be calculated with a five-day mean temporal resolution, whereas only monthly mean ocean velocity data are available directly as model output. Moreover, the use of geostrophic velocities rather than direct model output allows for a more

direct comparison with the altimetry dataset. More data processing steps are outlined in the Supplementary Notes. A visual representation of the velocity dataset (Fig. 1) demonstrates the effectiveness of the geostrophic velocity calculations and AWI-CM-1-1-MR in reproducing both overall surface flows and mesoscale activity. Supplementary Video 3 demonstrates this further through the animation of two sample years of velocity data.

To link EKE to other changes in the climate system, several additional variables were selected from model output and used to characterize the conditions surrounding simulated EKE change. Ocean velocity data (variables v_o and u_o) were used to calculate mean annual volume transport across chosen transects corresponding to currents that are hypothesized as physical drivers of EKE change (Extended Data Figs. 4 and 5). Transects were selected based on the published literature and to approximate the locations of in situ measurements of volume transport (Supplementary Table 4). The simulated stream function of AMOC at approximately 26° N and 1,040 m depth was also computed (Supplementary Table 4). Surface wind speed (variable $sfcWind$) was averaged across lines of latitude to assess change in the magnitude of mean zonal surface winds (Extended Data Fig. 7).

Satellite altimetry observations. To assist in the evaluation of simulated EKE, gridded geostrophic velocity anomaly observations (variables $ugosa$ and $vgosa$) between 1993 and 2020 from the Copernicus Marine Environment Monitoring Service and based on AVISO+ satellite altimetry were compared to the simulated data. The gridded observational data has a resolution of 0.25° by 0.25° and the equatorial band between 5° S and 5° N is replaced with approximated data⁴. The reference period used to compute anomalies in the altimetry dataset is 1993–2012. More information on processing of the altimetry dataset for this analysis can be found in the Supplementary Notes.

Eddy kinetic energy calculations

EKE can be defined as the energy contained by the time-varying component of ocean velocities, which are typically quantified as anomalies of ocean velocity. To account for potential changes in the mean state of ocean surface velocities in anomaly calculations, detailed in the Supplementary Notes, a running mean was removed from the raw data rather than a reference period mean. For each five-day period n in year j , a 21-year centred window of the same period n is considered from ten years prior, to ten years after year j . The ensemble mean of this window is then removed from the raw data to produce the anomaly as per equation (3). This method effectively filters both low-frequency and seasonal variability from the velocity data and interprets the remaining variability as the anomalies representative of eddy activity. Finally, velocity anomalies were used to calculate EKE as per equation (4). The ensemble mean of 21-year running means from each ensemble member represents 105 data points of reference surface velocity data intended to represent the mean state of surface flow while losing only ten years of data at the beginning and end of each time series. Due to internal variability, the ensemble members may differ slightly in their simulation of mean flow, but these differences are expected to be smaller than those stemming from seasonality or the effects of climate change, making an ensemble mean preferable for characterizing mean flow.

$$u_{n,j}' = u_{n,j} - \text{ENS}_{\text{avg}}(u_{n,j-10:j+10}) \quad (3)$$

$$\text{EKE}_{n,j} = \frac{1}{2} (u_{n,j}'^2 + v_{n,j}'^2) \quad (4)$$

where $\text{ENS}_{\text{avg}}()$ refers to the ensemble mean and prime ($'$) denotes an anomaly. For meridional velocity anomalies in equation (3), replace u with v .

The long-term analysis of modelled EKE takes advantage of the length of the dataset and an ensemble of simulations to address the

changing mean state of the global ocean due to anthropogenic climate change. To assess model fidelity, modelled data were compared to a shorter satellite altimetry dataset (1993–2020). For this comparison, anomalies of both datasets were calculated with respect to a 20-year reference period (1993–2012).

Time series of area-integrated EKE are produced by multiplying EKE by cell area and summing the results within selected basins (Extended Data Fig. 2). Basins were selected to encompass regions of high-eddy activity in the observed and modelled datasets both historically, and as it is projected at the end of the simulations, to capture spatial shifts. The resolution of the model grid was also considered when defining basins so that eddy-parameterizing regions are not included. Direct comparison of EKE in different ocean basins should be avoided, as lower (higher) area-integrated EKE may represent greater (lesser) eddy activity in a smaller (larger) area. This, along with the general underrepresentation of EKE compared with observations due to grid resolution, prompts the use of standardized EKE values based on mean and standard deviation of EKE during the observational period (equation (5)). This representation of EKE conveys change relative to conditions during the observed period (1993–2020) for each ensemble member and the observations respectively.

$$\text{EKE}_{i(\text{standardized})} = (\text{EKE}_i - \overline{\text{EKE}}) / \sigma_{\text{EKE}} \quad (5)$$

where i refers to a five-day mean time step, σ refers to the linearly detrended standard deviation during the observational period (1993–2020) and $\overline{\text{EKE}}$ refers to mean EKE during the observational period (1993–2020).

Characterization of change

Change in EKE within the observational record is typically assessed using linear trends^{10,18,20}. However, in the context of longer modelled datasets, the observational record becomes a mere snapshot of larger regimes of change, demonstrating the constraints of observation-based studies. The comprehensive modelled dataset is used to address several of these constraints. To account for the uncertainty regarding future GHG emissions and climate change mitigation, EKE trends are reported relative to MGST rise relative to a 1850–1899 mean, facilitating comparison with other emissions scenarios and grounding projections of future change in a more physical basis than temporal trends. To distinguish a robust climate change signal from natural variability, least-square linear trends relating EKE to MGST rise are calculated using data after the ensemble mean of an 11-year running mean of MGST anomalies surpasses a threshold of 1°K (Fig. 4). The spatial distribution of EKE change over time is quantified by subtracting historical EKE conditions (1860–1949) from conditions at the end of the century (2061–2090; Fig. 2c), capturing a period of approximately 3.3°K of warming, and the statistical significance of change was confirmed using a t -test (not shown). Together, these metrics should provide a reasonably comprehensive assessment of EKE change in the context of anthropogenic climate change.

Large-scale climatic conditions including volume transport, AMOC and southern hemisphere westerlies are reported to assist with the interpretation of EKE change relative to the broader effects of anthropogenic climate change. The probability density distributions of mean annual volume transport across selected transects and AMOC are reported for historical (1860–1949) and end-of-century projected (2061–2090) periods, along with the absolute and percentage changes (Extended Data Fig. 4 and Supplementary Table 4). Time series of the same volume transport and AMOC data are reported in Extended Data Fig. 5, and change in zonal mean surface wind speed between the same historical and projected periods is reported in Extended Data Fig. 7. Simple linear regression is used to assess the relationship between volume transport and EKE where relationships are expected based on the published literature (Extended Data Fig. 6). Regression analysis is applied to unfiltered volume transport, AMOC and EKE data and

low-pass-filtered data with a threshold of ten years to better identify relationships within high sub-decadal variability. The filtering was performed by applying Fourier transformations to the time series of each ensemble member, removing frequency signals greater than the 1/10 Hz threshold, applying an inverse Fourier transformation and discarding imaginary components.

Data availability

Geostrophic velocity anomalies derived from satellite altimetry anomalies are publicly available at <https://doi.org/10.48670/moi-00148>. Model output from AWI-CM-1-1-MR in the CMIP6 framework, including ocean velocity and surface wind is publicly available at <https://doi.org/10.22033/ESGF/CMIP6.359> (ref.³⁵). Daily sea surface height data used in this study is archived at the World Data Center for Climate at the DKRZ^{82,83}.

Code availability

The code used to calculate geostrophic velocities and eddy kinetic energy according to the methods described in this paper and to produce the main analysis figures is available on Github in the repository [awicm-cmip6-ekc](https://github.com/awicm-cmip6-ekc)⁸⁴.

References

- Hallberg, R. Using a resolution function to regulate parameterizations of oceanic mesoscale eddy effects. *Ocean Modell.* **72**, 92–103 (2013).
- Gent, P. R. & McWilliams, J. C. Isopycnal mixing in ocean circulation models. *J. Phys. Oceanogr.* **20**, 150–155 (1990).
- O'Neill, B. C. et al. The roads ahead: narratives for shared socioeconomic pathways describing world futures in the 21st century. *Glob. Environ. Change* **42**, 169–180 (2017).
- Moss, R. H. et al. The next generation of scenarios for climate change research and assessment. *Nature* **463**, 747–756 (2017).
- IPCC Summary for Policymakers. In *Climate Change 2021: The Physical Science Basis* (eds Masson-Delmotte, V. et al.) (Cambridge Univ. Press, 2021).
- Semmler, T. CMIP6_supplemental CMIP AWI AWI-CM-1-1-MR, *World Data Center for Climate (WDCC) at DKRZ*, <https://doi.org/10.26050/WDC/C6sCMAWAWM> (2022).
- Semmler, T. CMIP6_supplemental ScenarioMIP AWI AWI-CM-1-1-MR, *World Data Center for Climate (WDCC) at DKRZ*, <https://doi.org/10.26050/WDC/C6sSPAWAWM> (2022).
- Beech, N. n-beech/awicm-cmip6-ekc: 09-09-22 (v1.1). Jupyter notebooks to calculate and analyze eddy kinetic energy in AWI-CM-1-1-MR's CMIP6 simulations, *Zenodo*, <https://doi.org/10.5281/zenodo.7064462> (2022).

Acknowledgements

The work described in this paper has received funding from the Helmholtz Association through the project 'Advanced Earth System Model Capacity' (project leader: T.J., support code: ZT-0003) in the frame of the initiative 'Zukunftsthemen'. The content of the paper is the sole responsibility of the authors and it does not represent the opinion of the Helmholtz Association, and the Helmholtz Association is not responsible for any use that might be made of information contained. This work used resources of the Deutsches Klimarechenzentrum (DKRZ) granted by its Scientific Steering Committee (WLA) under project ID 995. The CMIP data used in this study were replicated and made available by the DKRZ. This work was supported by the European Union's Horizon 2020 collaborative project NextGEMS (grant number 101003470). This work was supported by the Helmholtz Climate Initiative REKLIM (Regional Climate Change) and the EPICA project in the research theme 'MARE:N—Polarforschung/MOSAIC' funded by the German

Federal Ministry for Education and Research with funding number O3F0889A.

Author contributions

N.B., T.J., T.R. and T.S. conceived the study. N.B. conducted the analysis and drafted the manuscript. Q.W. provided sample code for geostrophic velocity and ocean volume transport calculations. S.D. contributed to the discussion of variable-resolution meshes and their effects on eddies. All authors contributed to the scientific discussion, reviewed and contributed to the text of the manuscript.

Funding

The authors acknowledge support by the Open Access Publication Funds of Alfred Wegener Institute Helmholtz Center for Polar and Marine Research.

Competing interests

The authors declare no competing interests.

Additional information

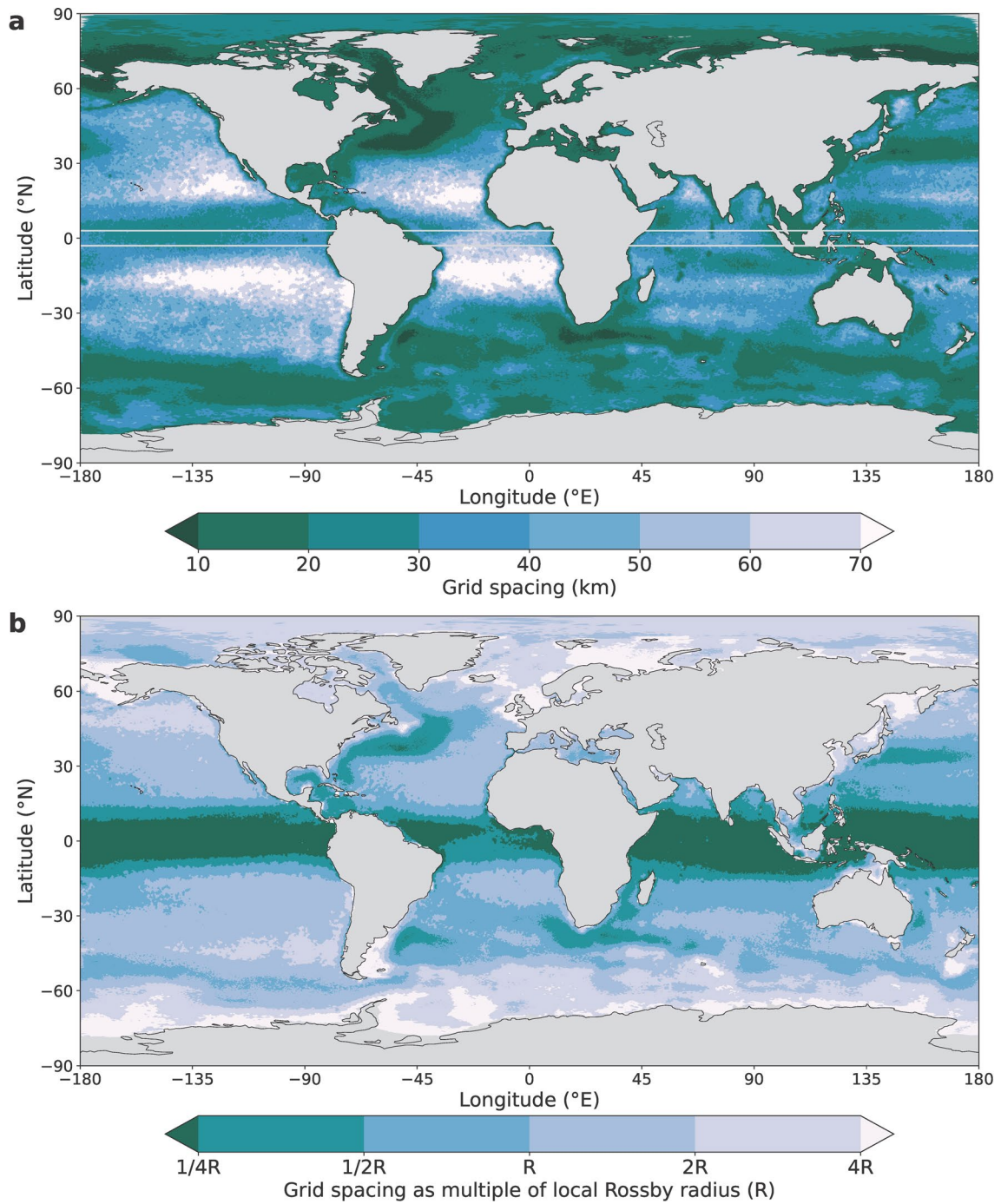
Extended data is available for this paper at <https://doi.org/10.1038/s41558-022-01478-3>.

Supplementary information The online version contains supplementary material available at <https://doi.org/10.1038/s41558-022-01478-3>.

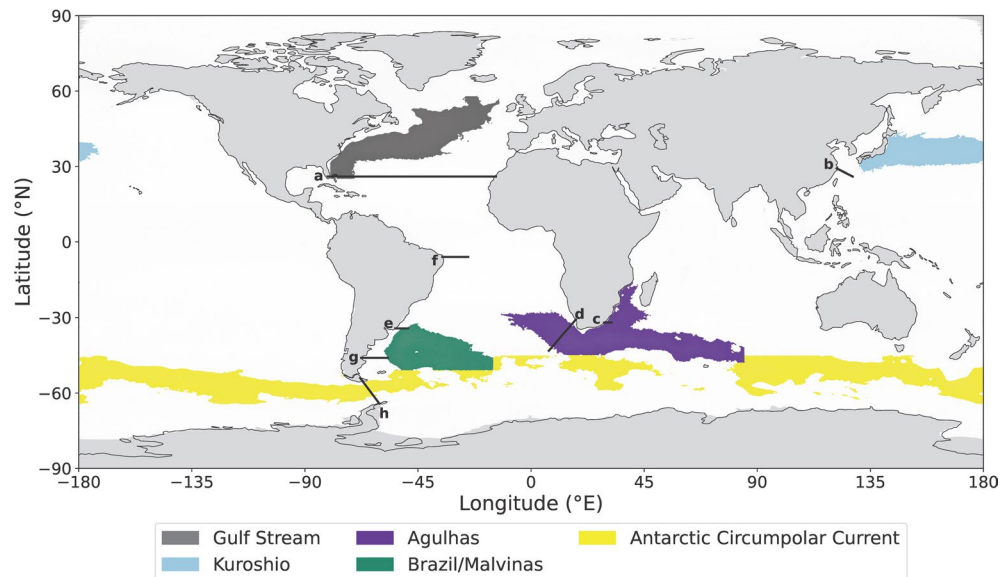
Correspondence and requests for materials should be addressed to Nathan Beech.

Peer review information *Nature Climate Change* thanks Josue Martinez-Moreno, Helene Hewitt and the other, anonymous, reviewer(s) for their contribution to the peer review of this work.

Reprints and permissions information is available at www.nature.com/reprints.



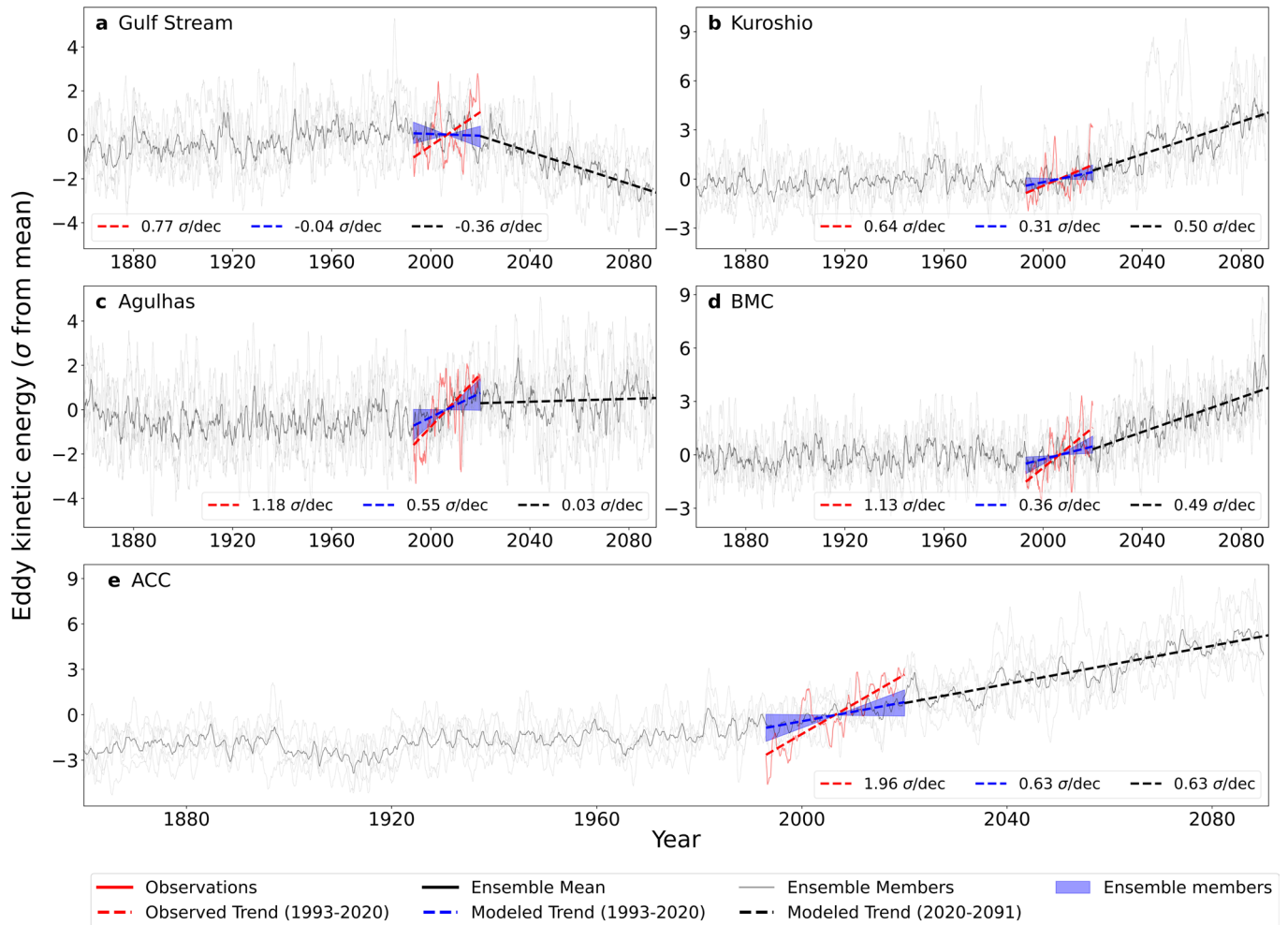
Extended Data Fig. 1 | Ocean grid resolution in AWI-CM-1-1-MR. Ocean grid resolution in AWI-CM-1-1-MR. (a) Grid resolution in units of kilometers. (b) Grid resolution relative to the local Rossby radius of deformation.



Extended Data Fig. 2 | Delimitations of ocean basins and transects.

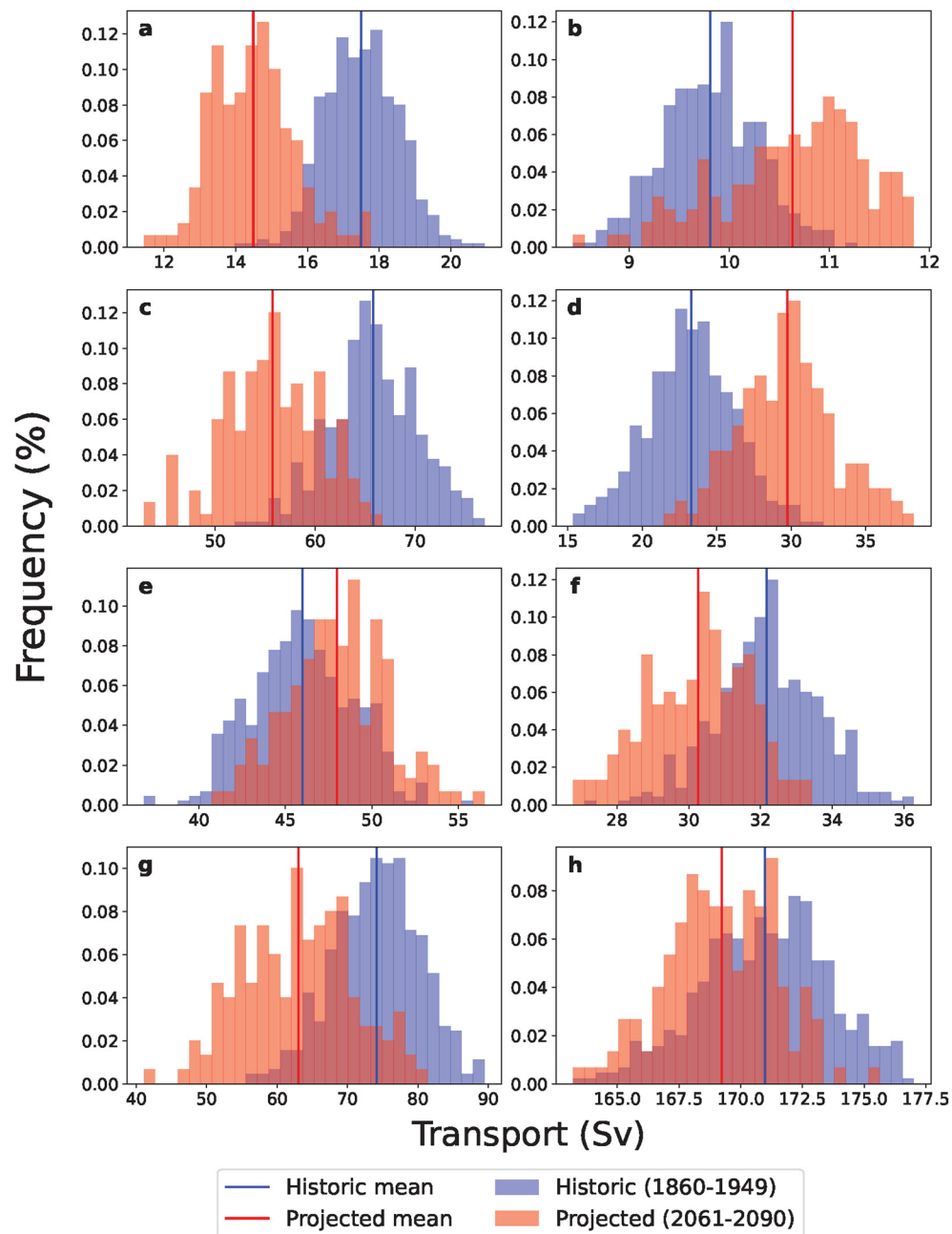
Delimitations of ocean basins and transects. The selected ocean basins used for analysis of area-integrated eddy kinetic energy are outlined in color. The transects over which ocean volume transport and AMOC are calculated are defined by black lines. More details regarding transects are available in

Supplementary Table 4. (a) AMOC. (b) Kuroshio Current volume transport. (c) Agulhas Current volume transport. (d) Agulhas Leakage. (e) Brazil Current volume transport. (f) North Brazil Current volume transport. (g) Malvinas Current volume transport. (h) Drake Passage throughflow.



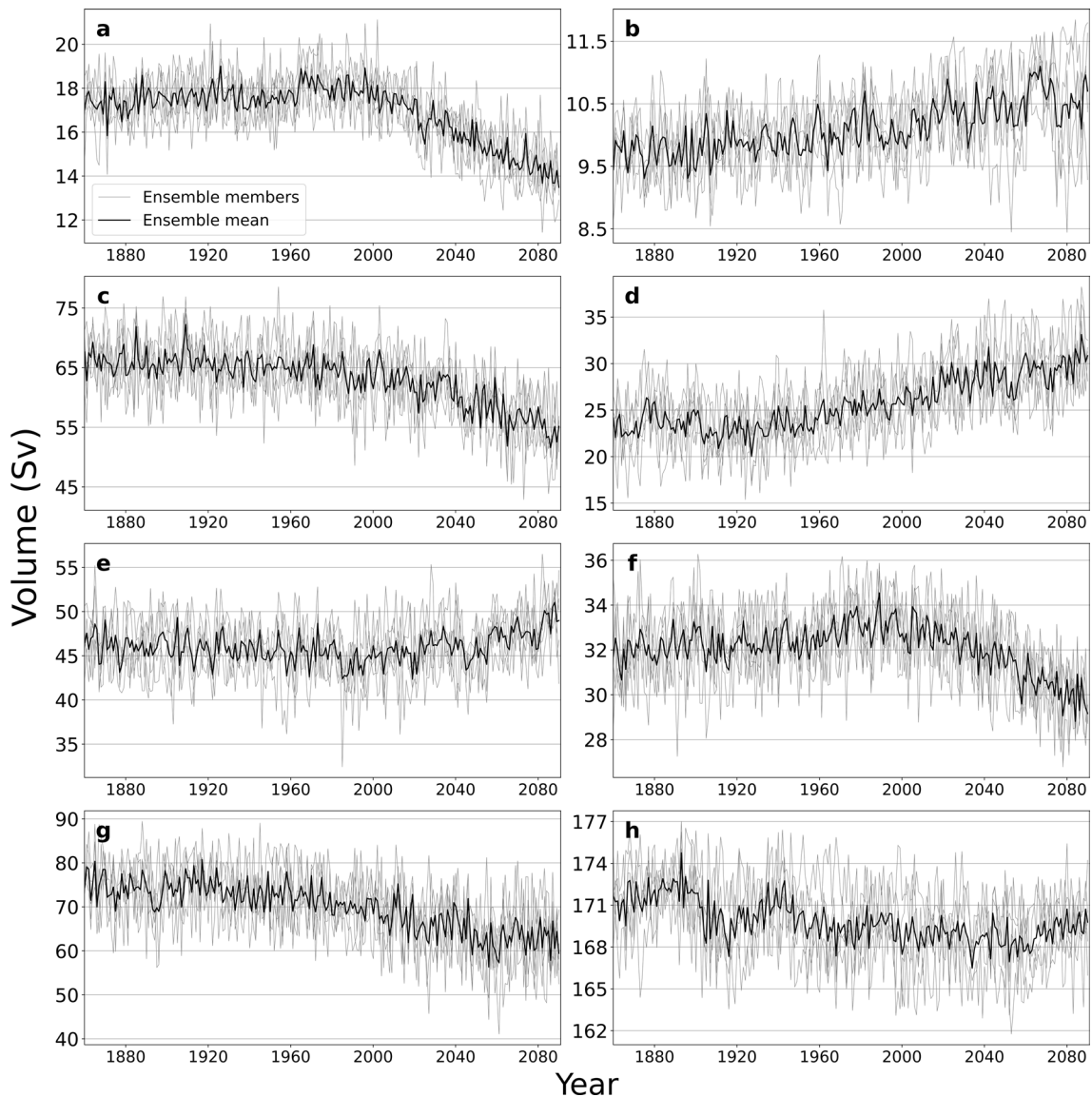
Extended Data Fig. 3 | Observed and simulated area-integrated regional eddy kinetic energy anomalies and trends. Observed and simulated area-integrated regional eddy kinetic energy anomalies and trends. Eddy kinetic energy anomalies are normalized relative to conditions during the observational period (1993–2020). Overlaid trends show the observed and simulated trends during

the observational period (1993–2020), ensemble range of simulated trends during the observational period (1993–2020), and ensemble mean trend after the observational period (2021–2090). (a) The Gulf Stream. (b) The Kuroshio Current. (c) The Agulhas Current. (d) The Brazil and Malvinas Currents. (e) The Antarctic Circumpolar Current.



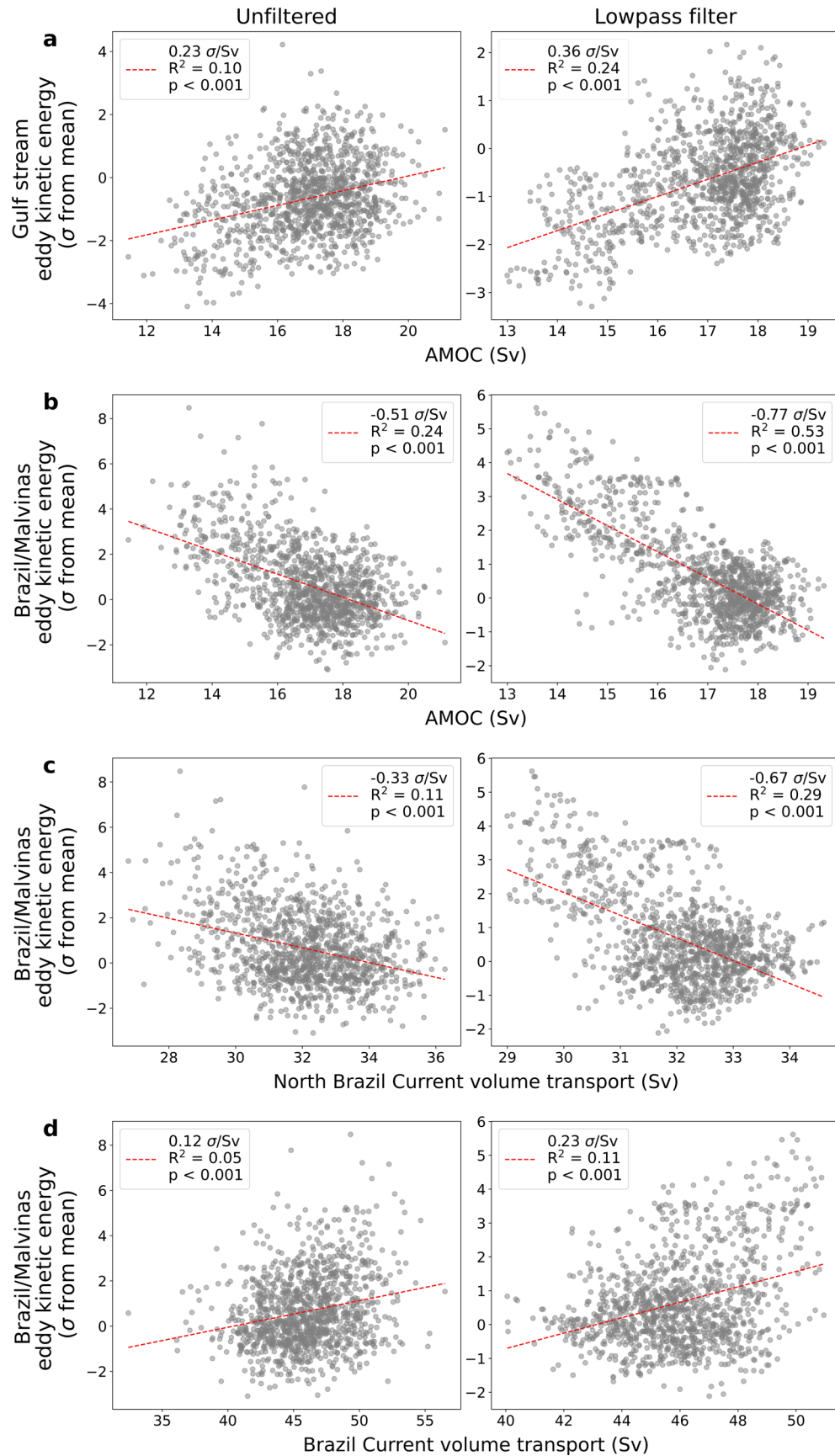
Extended Data Fig. 4 | Simulated distributions of volume transport and Atlantic meridional overturning circulation. Simulated distributions of volume transport and Atlantic meridional overturning circulation. Distribution of simulated annual volume transport through select ocean currents and Atlantic meridional overturning circulation during historical (1860–1949) and projected (2061–2090) periods. **(a)** Atlantic meridional overturning circulation.

(b) Kuroshio Current Volume transport. **(c)** Agulhas Current volume transport. **(d)** Agulhas leakage. **(e)** Brazil Current volume transport. **(f)** North Brazil Current volume transport. **(g)** Malvinas Current volume transport. Drake Passage throughflow. Details on the transects used to calculate volume transport can be found in Supplementary Table 4.



Extended Data Fig. 5 | Simulated annual volume transport through select ocean currents and Atlantic meridional overturning circulation. Simulated annual volume transport through select ocean currents and Atlantic meridional overturning circulation. **(a)** Atlantic meridional overturning circulation. **(b)** Kuroshio Current Volume transport. **(c)** Agulhas Current volume transport.

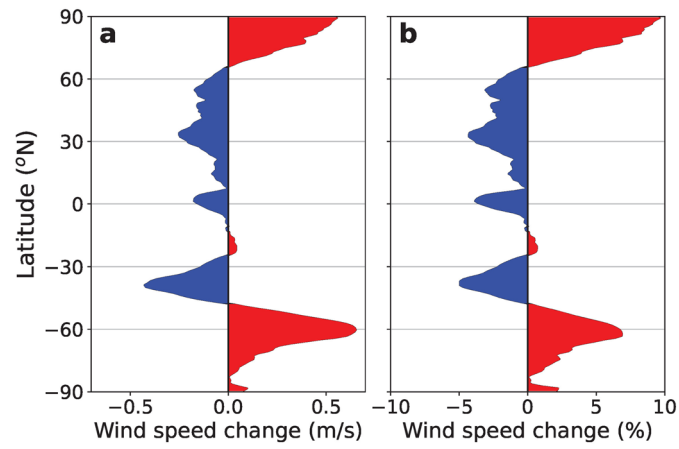
(d) Agulhas leakage. **(e)** Brazil Current volume transport. **(f)** North Brazil Current volume transport. **(g)** Malvinas Current volume transport. Drake Passage throughflow. Details on the transects used, integrated depths, and the definition of Atlantic meridional overturning circulation streamflow can be found in Supplementary Table 4.



Extended Data Fig. 6 | See next page for caption.

Extended Data Fig. 6 | Correlation between simulated area-integrated eddy kinetic energy in selected ocean basins and Atlantic meridional overturning circulation or simulated mean annual volume transport. Correlation between simulated area-integrated eddy kinetic energy in selected ocean basins and Atlantic meridional overturning circulation or simulated mean annual volume transport. Correlations are calculated with unfiltered data and with data filtered

to remove high-frequency variability with a threshold of 10 years. **(a)** Gulf stream eddy kinetic energy and Atlantic meridional overturning circulation. **(b)** Brazil/Malvinas Current eddy kinetic energy and Atlantic meridional overturning circulation. **(c)** Brazil/Malvinas Current eddy kinetic energy and North Brazil Current volume transport. **(d)** Brazil/Malvinas Current eddy kinetic energy and Brazil Current volume transport.



Extended Data Fig. 7 | Change in simulated zonally averaged global surface wind speed between historical (1860–1949) and projected (2061–2090) periods. Change in simulated zonally averaged global surface wind speed

between historical (1860–1949) and projected (2061–2090) periods. **(a)** Wind speed change in meters per second. **(b)** Wind speed change expressed as a percentage of the historical mean.